JACS
JOURNAL OF THE AMERICAN CHEMICAL SOCIETY
Article
pubs.acs.org/JACS

A Manganese(V)−Oxo Complex: Synthesis by Dioxygen Activation and Enhancement of Its Oxidizing Power by Binding Scandium Ion

Seungwoo Hong,[†] Yong-Min Lee,[†] Muniyandi Sankaralingam,[†] Anil Kumar Vardhaman,[†] Young Jun Park,[†] Kyung-Bin Cho,[†] Takashi Ogura,[‡] Ritimukta Sarangi,*[,§] Shunichi Fukuzumi,*[,†] and Wonwoo Nam*[,†]

[†]Department of Chemistry and Nano Science, Ewha Womans University, Seoul 03760, Korea
[‡]Picobiology Institute, Graduate School of Life Science, University of Hyogo, Hyogo 678-1297, Japan
[§]Stanford Synchrotron Radiation Lightsource, SLAC National Accelerator Laboratory, Menlo Park, California 94025, United States

Supporting Information

ABSTRACT: A mononuclear non-heme manganese(V)−oxo complex, $[Mn^{V}(O)(TAML)]^{-}$ (**1**), was synthesized by activating dioxygen in the presence of olefins with weak allylic C−H bonds and characterized structurally and spectroscopically. In mechanistic studies, the formation rate of **1** was found to depend on the allylic C−H bond dissociation energies (BDEs) of olefins, and a kinetic isotope effect (KIE) value of 16 was obtained in the reactions of cyclohexene and cyclohexene-d_{10}. These results suggest that a hydrogen atom abstraction from the allylic C−H bonds of olefins by a putative Mn^{IV}−superoxo species, which is formed by binding O_2 by a high-spin (S = 2) $[Mn^{III}(TAML)]^{-}$ complex, is the rate-determining step. A Mn(V)−oxo complex binding Sc^{3+} ion, $[Mn^{V}(O)(TAML)]^{-}$−(Sc^{3+}) (**2**), was also synthesized in the reaction of **1** with Sc^{3+} ion and then characterized using various spectroscopic techniques. The binding site of the Sc^{3+} ion was proposed to be the TAML ligand, not the Mn−O moiety, probably due to the low basicity of the oxo group compared to the basicity of the amide carbonyl group in the TAML ligand. Reactivity studies of the Mn(V)−oxo intermediates, **1** and **2**, in oxygen atom transfer and electron-transfer reactions revealed that the binding of Sc^{3+} ion at the TAML ligand of Mn(V)−oxo enhanced its oxidizing power with a positively shifted one-electron reduction potential (ΔE_{red} = 0.70 V). This study reports the first example of tuning the second coordination sphere of high-valent metal−oxo species by binding a redox-inactive metal ion at the supporting ligand site, thereby modulating their electron-transfer properties as well as their reactivities in oxidation reactions.

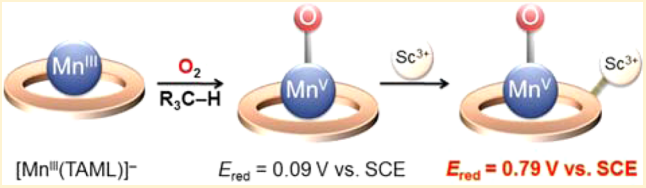

INTRODUCTION

High-valent manganese−oxo species have been invoked as key intermediates in the oxidation of organic substrates by manganese catalysts and in water oxidation by the oxygen-evolving complex in photosystem II (PS II).[1,2] In biomimetic studies, a large number of high-valent Mn(IV or V)−oxo complexes bearing porphyrin or non-porphyrin ligands have been synthesized and investigated intensively in various oxidation reactions.[1] For example, an X-ray crystal structure of a mononuclear non-heme Mn(V)−oxo complex bearing a tetraamido macrocyclic ligand (TAML) was reported by Collins and co-workers.[3] Other Mn(IV or V)−oxo complexes bearing non-heme ligands have been synthesized and investigated in oxidation reactions.[1a,4,5] In most cases, Mn−oxo complexes were synthesized using artificial oxidants, such as iodosylbenzene (PhIO) and hydroperoxides, but, to the best of our knowledge, there is only one report using dioxygen (O_2) as an oxidant for the generation of Mn(V)−oxo species under the condition of photoexcitation.[6]

In reactivity studies, effects of redox-inactive metal ions on the reactivities of metal−oxo complexes have attracted much attention,[1a,7−9] since the redox-inactive metal ions play important roles as cofactors in O_2-activation/formation reactions, such as Ca^{2+} ion in PS II.[2,10] In biomimetic studies, it has been demonstrated that binding of redox-inactive metal ions at the oxo group of metal−oxo species changes their chemical properties and reaction mechanisms in oxidation reactions.[7] In addition, it has been shown that the catalytic activity of metal complexes in oxidation reactions is increased greatly in the presence of redox-inactive metal ions.[11,12] The activation of O_2 by metal complexes is also shown to be facilitated in the presence of redox-inactive metal ions.[13] In those studies, the binding sites of redox-inactive metal ions were demonstrated or implied to be metal−oxo moieties.[7−13] However, the effect of redox-inactive metal ions on the second coordination sphere of metal−oxo complexes has been rarely investigated in oxidation reactions, especially in the case of binding of redox-inactive metal ions at supporting ligands.

Herein, we report the synthesis of a non-heme Mn(V)−oxo complex bearing a TAML ligand, $[Mn^{V}(O)(TAML)]^{-}$ (**1**, H_4TAML = tetraamido marcrocyclic ligand, 3,4,8,9-tetrahydro-

Received: April 15, 2016
Published: June 16, 2016

DOI: 10.1021/jacs.6b03874
J. Am. Chem. Soc. 2016, 138, 8523−8532

3,3,6,6,9,9-hexamethyl-1*H*-1,4,8,11-benzotetraazocyclotridecane-2,5,7,10(6*H*,11*H*)tetrone), by activating O_2 in the presence of a hydrogen atom (H atom) donor in the dark (Scheme 1); **1** was characterized by various spectroscopic

Scheme 1. Proposed Mechanisms for the Synthesis of Mn(V)−Oxo and Sc^{3+} Ion Bound Mn(V)−Oxo Complexes

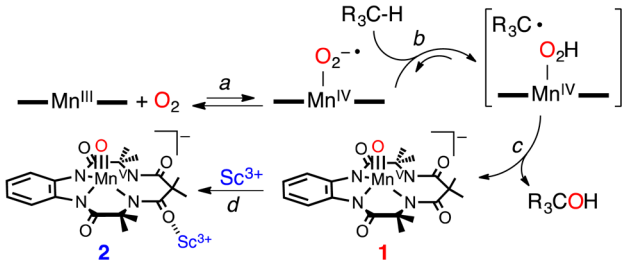

methods and X-ray crystallography. A non-heme Mn(V)−oxo complex binding Sc^{3+} ion, $[Mn^{V}(O)(TAML)]^{-}$−(Sc^{3+}) (**2**), was also synthesized by reacting **1** with Sc^{3+} ion (Scheme 1); the binding site of the Sc^{3+} ion was proposed to be the TAML ligand (vide infra). The reactivities of **1** and **2** were compared in oxygen atom transfer (OAT) and electron-transfer (ET) reactions to highlight the importance of the tuning of the second coordination sphere of metal−oxo species by binding a redox-inactive metal ion at the supporting ligand. The fundamental ET properties of **2**, such as the reorganization energy and the one-electron reduction potential, were determined and discussed as well.

RESULTS AND DISCUSSION

Generation and Characterization of 1. When a reaction solution containing $[Mn^{III}(TAML)]^{-}$ and cyclohexene was exposed to O_2 at room temperature, we observed the formation of a new intermediate (**1**) with an electronic absorption band at 430 nm (ε = 4000 M^{-1} cm^{-1}; Figure 1a) (Figure S1 for the characterization of $[Mn^{III}(TAML)]^{-}$; see also the section on Mechanistic Studies on Dioxygen Activation Reaction by $[Mn^{III}(TAML)]^{-}$ for the discussion of the formation mechanism of **1** in the presence of allylic C−H bonds). The intermediate **1** was highly stable at room temperature, allowing us to characterize it with various spectroscopic methods and X-ray crystallography. The electrospray ionization mass spectrum (ESI-MS) of **1** exhibited one prominent peak at m/z = 441.1, whose mass and isotope distribution pattern correspond to $[Mn^{V}(^{16}O)(TAML)]^{-}$ (**1**-^{16}O, calcd m/z = 441.1) (Figure 1b). When **1** was reacted with $^{18}O_2$, a mass peak corresponding to $[Mn^{V}(^{18}O)(TAML)]^{-}$ appeared at m/z = 443.1 (**1**-^{18}O, calcd m/z = 443.1). The X-band EPR and ^{1}H NMR spectra of **1** indicate that **1** is diamagnetic with a low-spin (S = 0) state (Figures S2 and S3), as reported in other Mn(V)−oxo complexes bearing TAML derivatives, corrole, porphyrin, and corrolazine.[3,14] The resonance Raman (rRaman) spectrum of **1**-^{16}O, recorded in CD_3CN at −40 °C with 407 nm laser excitation, showed one isotopically sensitive band at 977 cm^{-1}, which shifts to 937 cm^{-1} upon ^{18}O-substitution (Figure 1c). The observed isotopic shift of −40 cm^{-1} with ^{18}O-substitution is in good agreement with the calculated value for a diatomic Mn−O oscillator (−43 cm^{-1}). The calculated force constant for the 977 cm^{-1} mode by Hooke's law is 7.0 mdyn/Å, suggesting triple Mn−O bond character.[3c] The short Mn−O bond length of 1.5555(12) Å in the X-ray crystal structure of **1** (Figure 2a;

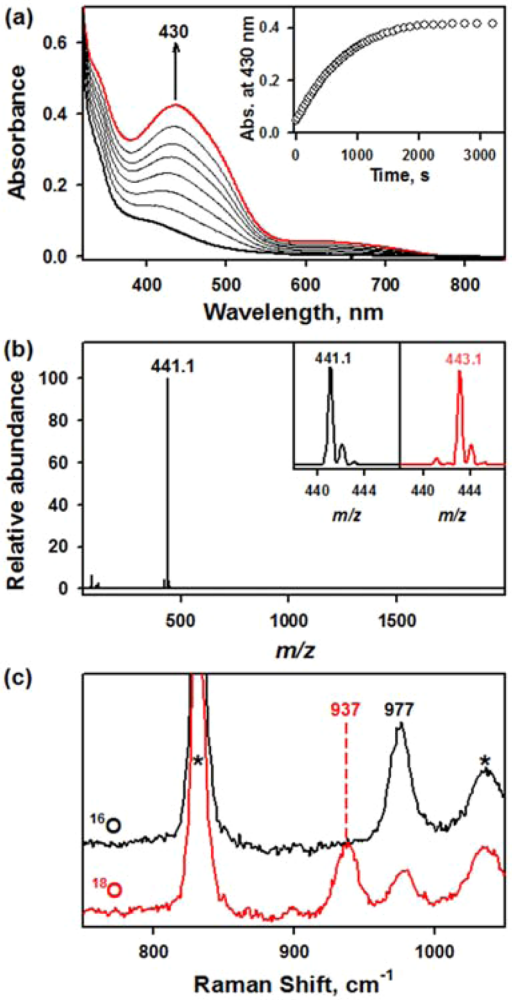

Figure 1. (a) UV−vis spectral changes observed in the reaction of $[Mn^{III}(TAML)]^{-}$ (0.10 mM) and O_2 in the presence of cyclohexene (10 mM) in acetone at 25 °C. Inset shows time trace monitored at 430 nm. (b) Negative mode ESI-MS spectrum of **1** generated in the O_2-activation reaction by $[Mn^{III}(TAML)]^{-}$ (0.10 mM) in the presence of cyclohexene (10 mM) in acetone at 25 °C. Insets show the observed isotope distribution patterns for **1**-^{16}O (left panel) and **1**-^{18}O (right panel, generated in $^{18}O_2$-saturated acetone). (c) rRaman spectra of **1**-^{16}O (4.0 mM, black line) and **1**-^{18}O (4.0 mM, red line) in CH_3CN at −40 °C upon 407 nm excitation. The peaks marked with * are from solvent.

see also Tables S1 and S2) is consistent with the Mn−O triple bond character as proposed in the rRaman experiments. Mn is in a slightly distorted square-pyramidal geometry, which arises from the axial oxo ligand and the four amido−N ligands (Mn−N average distance of 1.8926(14) Å). Taken together, **1** is a low-spin (S = 0) Mn^{V}−oxo complex with Mn−O triple bond character.[3b] It should be noted that **1** can also be generated in quantitative yield by reacting $[Mn^{III}(TAML)]^{-}$ with iodosylbenzene (PhIO) as an oxidant. The isolated **1** was then obtained by slow diffusion of Et_2O into a saturated CH_3CN solution of **1** and removal of the remaining PhIO and used for further studies.

Mechanistic Studies on Dioxygen Activation Reaction by $[Mn^{III}(TAML)]^{-}$. To give more insight into the O_2-activation reaction mechanism, one-electron oxidation potentials (E_{ox}) of $[Mn^{III}(TAML)]^{-}$ in two different solvent systems (i.e., CH_3CN and acetone) were determined by cyclic voltammetry (Figure

DOI: 10.1021/jacs.6b03874
J. Am. Chem. Soc. 2016, 138, 8523−8532

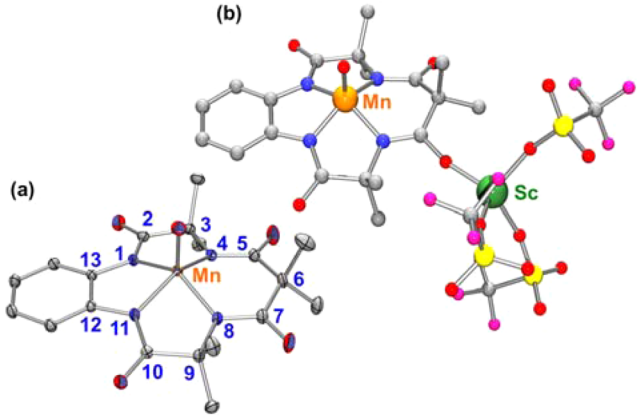

Figure 2. (a) X-ray crystal structure of **1** showing 50% probability ellipsoids. Tetraphenylphosphonium ion and hydrogen atoms are omitted for clarity. (b) DFT-calculated structure of **2** with Sc bound to the 7-position. Color for the structures: Mn, orange; Sc, green; N, blue; O, red; C, gray; S, yellow; F, pink.

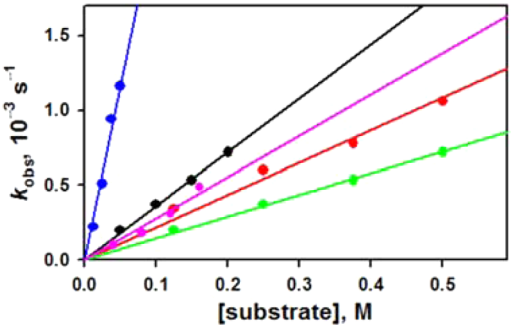

Figure 3. Plot of k_{obs} against the concentrations of cycloalkenes such as cyclohexene (blue circle), cycloheptene (black circle), cyclopentene (pink circle), cyclooctene (red circle), and cyclohexene-d_{10} (green circle) at 25 °C.

S1b). We found that the E_{ox} value of the Mn^{III} complex in CH_3CN was 0.45 V vs SCE, whereas the E_{ox} value in acetone was 0.35 V vs SCE. This result clearly indicates that the O_2-activation reaction may occur more favorably in acetone than in CH_3CN. The O_2-activation reaction indeed occurred in both solvent systems, but the formation rate of **1** in acetone was much faster than that in CH_3CN. We also carried out control experiments in which the reactions of the Mn^{III} complex with O_2 were performed in the absence of cycloalkenes with weak allylic C−H bonds in both CH_3CN and acetone. It is worth noting that the O_2-activation reaction does not occur in the absence of $[Mn^{III}(TAML)]^-$ or O_2 or cycloalkenes. To explore the possibility of an O_2-activation reaction through an autocatalytic radical chain pathway,[15] the O_2-activation reaction was carried out in the presence of DMPO (5,5-dimethyl-1-pyrroline *N*-oxide), which is a well-known spin trapping reagent.[16] However, even in the presence of 1.0% of DMPO, no induction period for the formation of **1** in the O_2-activation reaction by $[Mn^{III}(TAML)]^-$ was observed and the formation rates of **1** in the absence and presence of DMPO were the same, indicating that no autocatalytic radical chain pathway was involved in the O_2-activation reaction (Figure S4).

In kinetics studies, the formation rate of **1** was found to depend on the concentration of cyclohexene, and a second-order rate constant was determined to be 2.3×10^{-2} M^{-1} s^{-1} at 25 °C (Figure 3). We also found that the formation rate was correlated with the allylic C−H bond dissociation energies (BDEs) of olefins; the formation of **1** was faster with olefins having weak C−H BDEs, such as cyclohexene ($k_2 = 2.3 \times 10^{-2}$ M^{-1} s^{-1}, BDE = 81.0 kcal mol^{-1}), cycloheptene ($k_2 = 3.6 \times 10^{-3}$ M^{-1} s^{-1}, BDE = 83.0 kcal mol^{-1}), cyclopentene ($k_2 = 2.8 \times 10^{-3}$ M^{-1} s^{-1}, BDE = 84.7 kcal mol^{-1}), and cyclooctene ($k_2 = 2.1 \times 10^{-3}$ M^{-1} s^{-1}, BDE = 85.0 kcal mol^{-1}) (Figure 3; Figure S5).[17] In addition, the formation of **1** was slower in the reaction of cyclohexene-d_{10} (Figure 3), affording a kinetic isotope effect (KIE) value of 16. Moreover, the pseudo-first-order rate constants with the different concentrations of $[Mn^{III}(TAML)]^-$remained the same (Figure S6a), whereas the pseudo-first-order rate constant was proportional to the concentrations of cyclohexene (Figure 3) and O_2 (Figure S6b). Thus, the rate of formation of $[Mn^{V}(O)(TAML)]^-$ was given by the following equation: $d[Mn^{V}(O)]/dt = k_2([Mn^{III}]_0 - [Mn^{V}(O)])[cyclohexene][O_2]$. Because the rate exhibited first-order dependence with respect to concentration of the Mn^{III} complex, no bimetallic species (e.g., $Mn^{IV}-O_2-Mn^{IV}$)[18] are involved in the formation of the Mn^{V}−oxo complex. Products formed in the O_2-activation reactions by $[Mn^{III}(TAML)]^-$ with cyclohexene were analyzed by GC and GC−MS, showing that cyclohex-2-enol and cyclohex-2-enone were obtained as products with the yields of 21(3)% and 32(3)%, respectively (Figure S7).

When toluene was employed as a substrate, the formation of the Mn^{V}−oxo complex was too slow because of the relatively strong C−H bond of toluene (90 kcal mol^{-1}). When cyclohexadiene, which has a weaker C−H bond (BDE = 78 kcal mol^{-1}), was employed as a substrate, however, the rate constant ($k_2 = 3.6 \times 10^{-4}$ M^{-1} s^{-1}; Figure S8) was much slower than expected from the correlation with the BDE value. This may result from the much slower reaction of cyclohexadienyl radical with the Mn^{IV}−hydroperoxo complex as compared with the reaction of cyclohexenyl radical with the Mn^{IV}−hydroperoxo complex because of the reduced radical reactivity of more delocalized cylcohexadienyl radical. Such a delocalization effect was more pronounced in the reaction of hydroanthracenyl radical and the Mn^{IV}−hydroperoxo complex when the rate of the formation of the Mn^{V}−oxo complex with 9,10-dihydroanthracene (BDE = 77 kcal mol^{-1}) was too slow to be determined. Thus, substrates that we can use for the O_2 activation by $[Mn^{III}(TAML)]^-$ are limited to cycloalkenes with weak allylic C−H bonds.

Based on the kinetic studies discussed above, we conclude that the activation of allylic C−H bonds of olefins is the rate-determining step (rds) for the formation of **1** (Scheme 1, pathway *b*), and a mechanism is proposed as follows: A high-spin ($S = 2$) $[Mn^{III}(TAML)]^-$ complex binds O_2 to generate a Mn^{IV}−superoxo species (Scheme 1, pathway *a*),[19] followed by abstracting a H atom from an allylic C−H bond of olefin to form a putative Mn^{IV}−hydroperoxo species (Scheme 1, pathway *b*). Subsequently, a homolytic O−O bond cleavage of the Mn^{IV}−hydroperoxo species takes place to yield the Mn^{V}−oxo complex (Scheme 1, pathway *c*). This proposed mechanism is similar to the one that we reported recently in which non-heme Fe^{IV}−oxo complexes were formed in the reactions of Fe^{II} complexes and O_2 in the presence of olefins with weak allylic C−H bonds.[20]

Generation and Characterization of 2. Addition of 1.2 equiv of Sc^{3+} ion to a solution containing **1** in CH_3CN resulted in the formation of a Sc^{3+} ion bound Mn^{V}−oxo complex (**2**)

DOI: 10.1021/jacs.6b03874
J. Am. Chem. Soc. 2016, 138, 8523−8532

(Scheme 1, pathway *d*),[21] which exhibited a slightly red-shifted absorption band at 465 nm (ε = 4000 M^{-1} cm^{-1}) (Figure 4a,

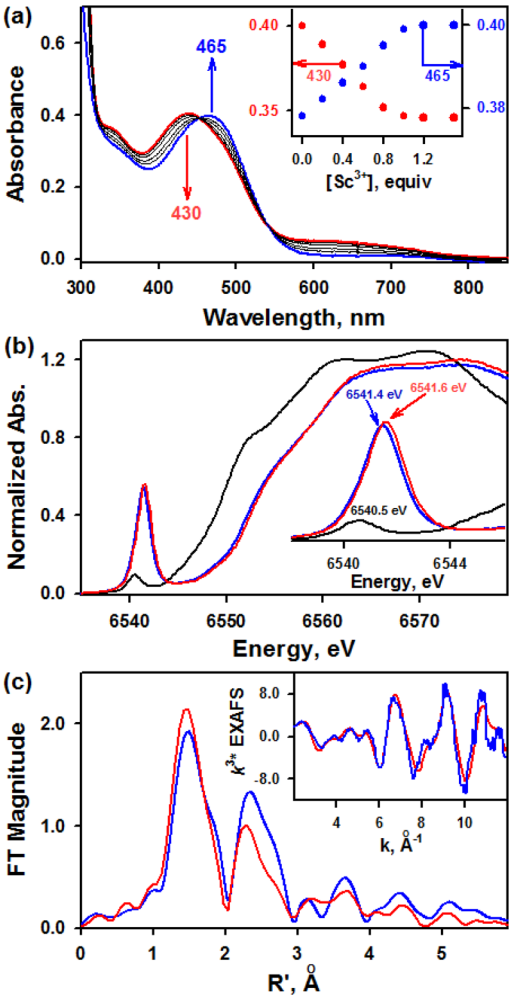

Figure 4. (a) UV−vis spectral changes showing the formation of **2** (blue line) and disappearance of **1** (0.10 mM, red line) upon addition of Sc^{3+} to **1** in increments of 0.2 equiv in CH_3CN at −20 °C. (b) The normalized Mn K-edge XAS data for $[Mn^{III}(TAML)]^-$ (black line), **1** (red line), and **2** (blue line). The inset shows the expanded pre-edge region. (c) A comparison of the non phase shift corrected Fourier transforms and the corresponding Mn K-edge EXAFS data (inset) for **1** (red line) and **2** (blue line).

blue line); unlike **1**, the intermediate **2** was metastable even at −20 °C ($t_{1/2}$ ∼ 2000 s). The spectroscopic titration at 465 nm for the formation of **2** as a function of the amount of Sc^{3+} ion added to the solution of **1** indicates that the stoichiometry of Sc^{3+} ion binding to Mn^V−oxo is 1:1 (Figure 4a, inset). The coordination of counteranions to the metal center was frequently observed in many X-ray crystal structures. It is also possible that the anion such as $CF_3SO_3^-$, which is originated from $Sc(CF_3SO_3)_3$, can coordinate to the Mn^V−oxo complex. To investigate this possibility, we independently added anions such as sodium trifluoromethanesulfonate ($NaCF_3SO_3$), sodium azide (NaN_3), and sodium thiocyanate (NaSCN) to the Mn^V−oxo complex. No visible spectral change was observed, indicating no binding of axial ligand to the Mn^V−oxo complex. We also added other weak Lewis acids such as Ca^{2+}, Zn^{2+}, and Sr^{2+}, however, the absorption band at 430 nm due to Mn^V−oxo complex remained without spectral change. This result suggested to us to assume that only strong Lewis acids are capable of binding to the present Mn^V−oxo complex.

Then, **2** was characterized by various spectroscopic methods such as coldspray ionization mass (CSI-MS), X-band EPR, ^1H NMR, rRaman, and X-ray absorption spectroscopies. A CSI-MS spectrum of **2** exhibited a mass peak at m/z = 932.9, whose mass and isotope distribution pattern correspond to $[Mn^V(^{16}O)(TAML)(Sc)(CF_3SO_3)_3]^-$ (**2**-^{16}O, calcd m/z = 932.9) (Figure S9a). When **2** was generated using **1**-^{18}O, a mass peak assignable to $[Mn^V(^{18}O)(TAML)(Sc)(CF_3SO_3)_3]^-$ appeared at m/z = 934.9 (**2**-^{18}O, calcd m/z = 934.9). The X-band EPR and ^1H NMR spectra revealed that **2** is diamagnetic with a low-spin (S = 0) state (Figures S3c and S9b). The rRaman spectrum of **2**-^{16}O, recorded in CD_3CN at −40 °C with 407 nm laser excitation, showed one isotopically sensitive band at 976 cm^{-1}, which shifts to 936 cm^{-1} upon ^{18}O-substitution (Figure S9c); it is notable that the rRaman bands are almost identical to those of the **1**-^{16}O and **1**-^{18}O (Figure 1c).

The normalized Mn K-edge XAS spectra of the starting material $[Mn^{III}(TAML)]^-$, **1**, and **2** are presented in Figure 4b. The inset shows the expanded pre-edge region. The pre-edge feature corresponding to the electric dipole allowed, quadrupole forbidden, 1s → 3d transition occurs at 6540.5 eV for $[Mn^{III}(TAML)]^-$, shifts to higher energy by 1.1 eV, and occurs at 6541.6 eV for **1**. The intensity of the pre-edge feature increases by ∼7-fold on going from $[Mn^{III}(TAML)]^-$ to **1**. This increase in energy and intensity of the pre-edge feature indicates an increase in covalency and the presence of a very short Mn−O interaction in **1**. On going from $[Mn^{III}(TAML)]^-$ to **1**, the rising edge shifts from 6549.5 to 6553.4 eV, an increase of 3.9 eV, consistent with an increase in charge on the Mn center in **1**. These spectral features observed for **1** are consistent with other reported 5-coordinate Mn^VO systems,[22] confirming the $[Mn^V(O)(TAML)]^-$ nature of **1**. A comparison of the Mn K-edge XAS spectra (Figure 4b) of **1** and **2** shows that, upon Sc^{3+} binding, both the intensity and energy position of the pre-edge feature decrease slightly, indicating a modest perturbation in ligand field strength arising from Sc^{3+} binding.

Figure 4c shows a comparison of the non phase shift corrected Mn K-edge EXAFS Fourier transform data for **1** and **2**. The inset shows the EXAFS region (k = 2−11.9 $Å^{-1}$). Small differences in both EXAFS and FT data are observed. Specifically, on going from **1** to **2**, the peak at R' ∼ 1.5 Å shifts to higher R' values and decreases in intensity. Furthermore, the intensity of the features between R' ∼ 2 and 3 Å increases in **2** relative to **1**. FEFF fits to the data of **1** (Figure 4c, red line; Figure S10a) reveal a short Mn−O interaction at 1.54 Å and 4 Mn−N interactions at 1.89 Å. The second and third shells are fitted with single and multiple scattering components from the TAML ligand. FEFF fits to the data for **2** reveal only a slight elongation of the Mn−O distance to 1.57 Å and 4 Mn−N interactions at 1.91 Å (Figure 4c, blue line; Figure S10b). The second and third shells are fitted with single and multiple scattering components from the TAML ligand but with overall low σ^2 values and increase in degeneracy of a 3.96 Å Mn−C interaction (8 in **2** compared with 4 in **1**; Table S4). These differences to the second and third shells indicate a stronger back scattering contribution by the TAML ligand upon Sc^{3+} binding.

The experimentally obtained structure of **2** was compared to the DFT-optimized structure (Figure 2b; see also Experimental Section for computational details). As a calibration, calculations

DOI: 10.1021/jacs.6b03874
J. Am. Chem. Soc. 2016, 138, 8523−8532

were done on **1** where the calculations yielded Mn−O and Mn−N(average) distances of 1.57 and 1.90 Å, respectively, in good agreement with both the crystal structure and EXAFS data. In calculations, the Mn−O vibration frequency was seen at 1017 cm^{-1} (Table S5). This frequency shifted 44 cm^{-1} to 973 cm^{-1} upon ^{18}O substitution. Note that these frequencies are, contrary to the usual practice, not scaled, as a scaling factor is not available for our exact calculation setup (B3LYP/LACVP in solvent, see DFT Methods). However, if we were to use a scaling factor of 0.962, as obtained at the very similar[23] B3LYP/6-31G level calculations,[24] the obtained frequency would be at 978 cm^{-1} shifting to 936 cm^{-1}, in agreement with experiments. The TD-DFT calculated spectrum for this species (Figure S11a) exhibited a peak at 448 nm, reasonably close to the experimentally determined peak at 430 nm. This peak represents a collection of electron transitions from the ligand as well as the Mn d_{xy} orbital to the other Mn d-orbitals. There is also a minor peak at 668 nm, also seen in Figure 1a. Thus, we conclude that the calculations sufficiently reproduce the experiments for species **1**.

Addition of $Sc(CF_3SO_3)_3$ was then done on three different possible oxygen positions, namely, the Mn−oxo, the 7-one, and the 10-one positions of TAML (see Figure 2a for the positions). Adding $Sc(CF_3SO_3)_3$ to the Mn−oxo position generated two energetically similar $S = 0$ species, one being a closed shell and the other an open shell configuration (Tables S6−S8). However, these structures were on the order of 10 kcal/mol higher up in energy than the TAML ligand-bound alternatives. Also, the Mn−O distances were significantly elongated upon Sc^{3+} ion binding to 1.72 and 1.68 Å for open and closed shells, respectively, neither of which is in agreement with the EXAFS results on **2**. In addition, the calculated Mn−O vibration is now found mixed with other vibrations at 768 and 788 cm^{-1}, very much off from the experimentally determined 977 cm^{-1}. The TD-DFT calculated UV spectrum also exhibits multiple peaks above 500 nm (Figure S11b), which are not seen experimentally. It is therefore more likely that the Sc^{3+} ion binding occurs at the TAML ligand and, more specifically, to the 7-one position, as this is 1.42 kcal/mol lower in energy than binding to the 10-one position (see Figure 2b for the DFT-calculated structure). The TD-DFT spectrum shows a peak at 482 nm (Figure S11c), showing that the peak has shifted 34 nm upon Sc^{3+} binding, as compared to 35 nm experimentally in Figure 4a. This proposed binding site of the Sc^{3+} ion in **2** was confirmed by ^1H NMR spectra of **1** and **2** taken at −20 °C (Figure S3); the methyl peak at the 6-position of TAML ligand was shifted the most upon addition of Sc^{3+} ion, whereas the benzene and methyl peaks at 3- and 9-positions of TAML shifted moderately. Thus, ^1H NMR analysis together with rRaman data (vide supra) indicates that the Sc^{3+} ion binds close to the 6-position (e.g., at 5 or 7 carbonyl oxygen), as shown in the DFT-determined structure of **2** (Figure 2b).

Reactivity Comparison between 1 and 2. The reactivities of **1** and **2** were compared in OAT and ET reactions, to understand the effect of Sc^{3+} ion on the reactivity of the Mn^V−oxo species. In OAT reactions, **1** disappeared with a first-order rate profile upon addition of triphenylphosphine (PPh_3), and a second-order rate constant (k_2) of 1.2×10^{-1} M^{-1} s^{-1} was obtained at 25 °C (Figure S12). In the reaction of **2** and PPh_3, a second-order rate constant (k_2) was determined at −20 °C due to the much greater reactivity of **2** compared to that of **1**, and it was 1.1×10^2 M^{-1} s^{-1} from the slope of pseudo-first-order rate constants against PPh_3 concentrations (Figure S13). This result demonstrates that the reactivity of **2** is much greater than that of **1** in the OAT reaction (i.e., $>10^4$ times by considering the temperature difference). A similar result was reported previously by using Mn^V−oxo complex bearing an analogue of TAML ligands.[3b] The electrophilic reactivities of **1** and **2** were also investigated in the oxidation reactions of *para*-substituted PPh_3 derivatives, such as $(p\text{-Cl-Ph})_3P$ and $(p\text{-Me-Ph})_3P$. In both cases of **1** and **2**, reactivity increased with decrease of one-electron oxidation potential (E_{ox}) of PPh_3 derivatives, indicating that **1** and **2** act as an electrophile in the oxidations of PPh_3 derivatives (Figures S14 and S15). In the oxidation of PPh_3 by **1** and **2**, $Ph_3P{=}O$ was obtained as a sole product with >90% yields. The Mn product obtained in the reactions between **1** or **2** and PPh_3 was determined to be $[Mn^{III}(TAML)]^-$ (Figures S16 and S17).

In ET reactions, $[Mn^V(O)(TAML)]^-$ (**1**) did not react with 1,1′-dimethylferrocene (Me_2Fc; E_{ox} = 0.26 V vs SCE), but reacted with octamethylferrocene (Me_8Fc; E_{ox} = −0.04 V vs SCE) and decamethylferrocene ($Me_{10}Fc$; E_{ox} = −0.08 V vs SCE) in CH_3CN at 25 °C (Figure S18), indicating that one-electron reduction potential of **1** is between 0.26 and −0.04 V vs SCE. This was also confirmed by cyclic voltammetry, providing that the E_{red} of **1** is 0.09 V vs SCE (Figure S19), which is consistent with the results of ET reactions. However, Mn^V−O−Sc^{3+} (**2**) reacted with a series of one-electron donors such as ferrocene (Fc; Figure 5) and its derivatives in CH_3CN

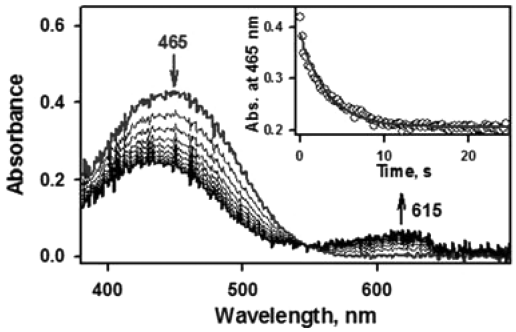

Figure 5. UV−vis spectral changes observed in the reaction of **2** (0.10 mM) with Fc (1.25 mM) in CH_3CN at −20 °C. Inset shows time trace monitored at 465 nm due to **2**.

at −20 °C. This result indicates that **2** is a much stronger one-electron oxidant than **1**, which is consistent with the greater reactivity of **2** in the OAT reaction (vide supra). The ET reactions between **2** and Fc derivatives were followed by monitoring disappearance of the absorption band at 465 nm due to **2**, with the concomitant appearance of absorption band in the range of 600−800 nm due to ferrocenium ion (Fc^+) and its derivatives (Figure 5; Figure S20). The stoichiometry in the reaction of **2** and Fc was 1:1, because only 1 equiv of Fc^+ ion was formed in the pseudo-first-order conditions (Figure 5). In addition, Mn(IV) ion was detected as a final Mn product by X-band EPR after the completion of ET reaction between **2** and Fc (Figure S21). ET reduction of **2** was also found to be in equilibrium with Br_2Fc (E_{ox} = 0.71 V vs SCE) (eq 1),[25] where the final concentration of Br_2Fc^+ produced in the ET of **2** increases with increasing the initial concentration of Br_2Fc (Figure 6a). The equilibrium constant (K_{et}) was determined to be 47 in CH_3CN at −20 °C (Figure S22). The apparent one-electron reduction potential (E_{red}) of **2** was then determined to be 0.79 V vs SCE from the K_{et} value and E_{ox} value of Br_2Fc

DOI: 10.1021/jacs.6b03874
J. Am. Chem. Soc. 2016, 138, 8523−8532

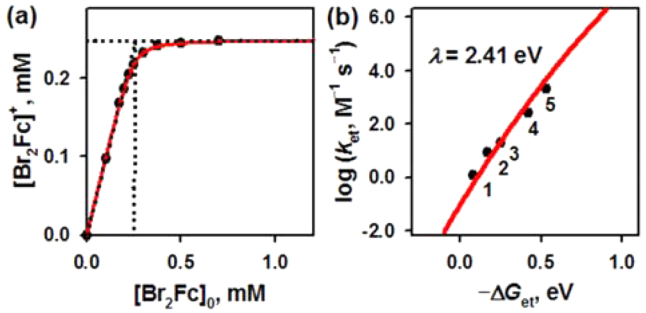

Figure 6. (a) Plot of concentration of Br_2Fc^+ produced in ET from Br_2Fc to **2** (0.25 mM) against initial concentration of Br_2Fc, $[Br_2Fc]_0$. (b) Driving force ($-\Delta G_{et}$) dependence of the logarithm of the rate constants (log k_{et}) of ET from one-electron donors (1, Br_2Fc; 2, BrFc; 3, AcFc; 4, Fc; 5, Me_2Fc) to **2** in CH_3CN at −20 °C.

using the Nernst equation (eq 2). This result is in good agreement with the electrochemically determined E_{red} of **2** (Figure S19c). Thus, the E_{red} value of **2** is largely more positive than **1** (ΔE_{red} = 0.70 V). Similar results were reported in $[Mn^{IV}(O)(N4Py)]^{2+}$ (0.80 V vs SCE) and its Sc^{3+} ion bound complex, $[Mn^{IV}(O)(N4Py)]^{2+}-(Sc^{3+})_2$ (1.42 V vs SCE).[7c]

$$[Mn^{V}(O)(TAML)]^{-} - (Sc^{3+}) + Br_2Fc \overset{K_{eq}}{\rightleftharpoons} [Mn^{IV}(O)(TAML)]^{2-} - (Sc^{3+}) + Br_2Fc^{+} \quad (1)$$

$$E_{red} = E_{ox} + (RT/F) \ln K_{et} \quad (2)$$

The ET rate obeyed pseudo-first-order kinetics in the presence of large excess of Fc derivatives. The second-order rate constants (k_{et}) were determined from the slopes of linear plots of k_{obs} against the concentrations of Fc derivatives (Figure S23). The k_{et} values of various reductants were summarized in the Table 1, along with the E_{ox} values of the reductants, and

Table 1. Oxidation Potentials (E_{ox}) of Electron Donors, Rate Constants (k_{et}), and Driving Force ($-\Delta G_{et}$) for One-Electron Reduction of 2 by Electron Donors in CH_3CN at −20 °C

electron donor	E_{ox},[a] V vs SCE	k_{et}, M^{-1} s^{-1}	$-\Delta G_{et}$, eV
dimethylferrocene (Me_2Fc)	0.26	1.7×10^3	0.53
ferrocene (Fc)	0.37	2.1×10^2	0.42
bromoferrocene (BrFc)	0.54	1.8×10	0.25
acetylferrocene (AcFc)	0.62	1.2×10	0.17
dibromoferrocene (Br_2Fc)	0.71	1.3	0.08

[a]Taken from ref 25.

driving force of ET [$-\Delta G_{et} = e(E_{red} - E_{ox})$ in eV, where e is the elementary charge]. The driving force dependence of the logarithm of the rate constants of ET from Fc derivatives to **2** in CH_3CN at −20 °C is shown in Figure 6b, in which the log k_{et} values are plotted against the $-\Delta G_{et}$ values. The curve is well suited by the red solid line in Figure 6b in light of the Marcus theory of adiabatic outer-sphere ET (eq 3),[26]

$$k_{et} = Z \exp[-(\lambda/4)(1 + \Delta G_{et}/\lambda)^2/k_B T] \quad (3)$$

in which Z is the collision frequency taken as 1×10^{11} M^{-1} s^{-1}, λ is the reorganization energy of ET, k_B is the Boltzmann constant, and T is the absolute temperature. Thus, the λ value of 2.41 eV was determined using eq 3. It is of interest to note that the λ value of **2** is slightly higher than those of other Sc^{3+} ion bound Mn^{IV}–oxo complexes (2.12–2.21 eV),[7c] but lower than those of non-heme Fe^{IV}–oxo complexes.[27]

CONCLUSION

To close, we have presented the synthesis and spectroscopic and structural characterization of a mononuclear non-heme Mn^{V}–oxo complex and its Sc^{3+} ion bound Mn^{V}–oxo complex. The Mn^{V}–oxo complex was synthesized by activating dioxygen in the presence of olefins with weak allylic C–H bonds. We have proposed a mechanism as follows: A putative Mn^{IV}–superoxo species, which is formed by binding O_2 by a high-spin (S = 2) $[Mn^{III}(TAML)]^{-}$ complex, abstracts a hydrogen atom from the allylic C–H bonds of olefins to form a putative Mn^{IV}–hydroperoxo species (Scheme 1, pathways *a* and *b*), followed by a homolytic O–O bond cleavage of the Mn^{IV}–hydroperoxo species to yield the Mn^{V}–oxo complex (Scheme 1, pathway *c*). The Mn^{V}–oxo complex was characterized with various spectroscopic methods and X-ray crystallography. Then, the reaction of the Mn^{V}–oxo complex with 1 equiv of Sc^{3+} ion produced a Mn^{V}–oxo complex binding a Sc^{3+} ion (Scheme 1, pathway *d*). We have proposed that the Sc^{3+} ion is bound to the TAML ligand, not to the Mn–oxo moiety. This is probably due to the low basicity of the oxo group in Mn^{V}–oxo, compared to the basicity of the amide carbonyl group in the TAML ligand. Their reactivities in OAT and ET reactions demonstrate that the binding of Sc^{3+} ion at the TAML ligand of Mn^{V}–oxo markedly enhances its oxidizing power with a largely positively shifted one-electron reduction potential. Thus, the redox-inactive metal ion binding at the supporting ligand or at the metal–oxo moiety changes reactivities of metal–oxo species in OAT and ET reactions greatly. To the best of our knowledge, this study reports the first example of a redox-inactive metal ion induced tuning of the second coordination sphere of metal–oxo species that modulates their electrochemical properties as well as their reactivities in oxidation reactions.

EXPERIMENTAL SECTION

Materials. Commercially available chemicals were used without further purification unless otherwise indicated. Solvents were dried according to published procedures and distilled under Ar prior to use.[28] Iodosylbenzene (PhIO) was prepared by a literature method.[29] TAML-H_4 ligand was purchased from GreenOx Catalysts Inc. (USA). $^{18}O_2$ (98% ^{18}O-enriched) and $H_2{}^{18}O$ (95% ^{18}O-enriched) were purchased from ICON Services Inc. (Summit, NJ, USA). The starting Mn(III) complex, $Li(CH_3OH)_2[Mn^{III}(TAML)(CH_3OH)]$, was prepared according to the literature.[30] The cation exchange from Li^+ to PPh_4^+ was also performed by adding 10 eqiuv of PPh_4Cl to a solution of $Li(CH_3OH)_2[Mn^{III}(TAML)(CH_3OH)]$ in order to increase the solubility of $[Mn^{III}(TAML)]^{-}$ in CH_3CN.[3b] The reaction solution was filtered and used for further characterization studies.

Instrumentation. UV–vis spectra were recorded on a Hewlett-Packard Agilent 8453 UV–visible spectrophotometer equipped with a circulating water bath or a UNISOKU cryostat system (USP-203; UNISOKU, Japan). Electrospray ionization mass spectra (ESI-MS) were collected on a Thermo Finnigan (San Jose, CA, USA) LCQ Advantage MAX quadrupole ion trap instrument, by infusing samples directly into the source at 20 μL/min using a syringe pump. The spray voltage was set at 4.7 kV and the capillary temperature at 120 °C. Cold spray ionization mass spectra (CSI-MS) data were collected on a JMS-T100CS (JEOL) mass spectrometer equipped with a CSI source. Typical measurement conditions are as follows: needle voltage, 2.2 kV; orifice 1 current, 50–500 nA; orifice 1 voltage, 0 to 20 V; ring lens voltage, 10 V; ion source temperature, 5 °C; spray temperature, − 40 °C. X-band CW-EPR spectra were recorded at 5 K using an X-band Bruker EMX-plus spectrometer equipped with a dual mode cavity (ER

DOI: 10.1021/jacs.6b03874
J. Am. Chem. Soc. 2016, 138, 8523–8532

4116DM). Low temperatures were achieved and controlled with an Oxford Instruments ESR900 liquid He quartz cryostat with an Oxford Instruments ITC503 temperature and gas flow controller. The experimental parameters for EPR spectra were as follows: Microwave frequency = 9.646 GHz, microwave power = 1.0 mW, modulation amplitude = 10 G, gain = 1×10^4, modulation frequency = 100 kHz, time constant = 40.96 ms, and conversion time = 85.00 ms. ^{1}H NMR spectra were measured with a Bruker model digital AVANCE III 400 FT-NMR spectrometer. Resonance Raman spectra were obtained using a liquid nitrogen cooled CCD detector (CCD-1024×256-OPEN-1LS, HORIBA Jobin Yvon) attached to a 1 m single polychromator (MC-100DG, Ritsu Oyo Kogaku) with a 1200 groove/mm holographic grating. Excitation wavelength of 407.0 nm was provided by He−Cd laser (Kimmon Koha, IK5651R-G and KR1801C) with 20 mW power at the sample point. All measurements were carried out with a spinning cell (1000 rpm) at −40 °C. Raman shifts were calibrated with indene, and the accuracy of the peak positions of the Raman bands was ±1 cm^{-1}. Electrochemical measurements were performed on a CHI630B electrochemical analyzer (CH Instruments, Inc.) in deaerated CH_3CN containing 0.10 M Bu_4NPF_6 ($TBAPF_6$) as a supporting electrolyte at −40 °C. A conventional three-electrode cell was used with a platinum working electrode (surface area of 0.30 mm^2), a platinum wire as a counter electrode, and an Ag/Ag$^+$ electrode as a reference electrode. The platinum working electrode was routinely polished with BAS polishing alumina suspension and rinsed with acetone and acetonitrile before use. The measured potentials were recorded with respect to an Ag/Ag$^+$ (0.010 M) reference electrode. All potentials (vs Ag/Ag$^+$) were converted to values vs SCE by adding 0.29 V.[31] All electrochemical measurements were carried out under Ar atmosphere. Product analysis was performed with Agilent Technologies 6890N gas chromatograph (GC). Quantitative analyses were made on the basis of comparison of GC peak integration between products and authentic samples.

Generation of Non-Heme Mn^V(O) Intermediate, 1 and 2. The non-heme Mn^V(O) complex, [Mn^V(O)(TAML)]$^-$ (**1**), was generated by reacting Li(CH$_3$OH)$_2$[Mn^{III}(TAML)(CH$_3$OH)] or (PPh$_4$)-[Mn^{III}(TAML)] (0.10 mM) with dioxygen (O_2) in the presence of cycloalkenes (10−500 mM), such as cyclopentene, cyclohexene, cycloheptene, cyclooctene, and cyclohexene-d_{10}, in acetone at 25 °C. ^{18}O-labeled **1** was prepared under identical reaction conditions using $^{18}O_2$ in acetone at 25 °C. Alternatively, **1** was also prepared by reacting Li(CH$_3$OH)$_2$[Mn^{III}(TAML)(CH$_3$OH)] (52.8 mg, 0.10 mmol) with excess solid iodosylbenzene (PhIO) in CH_3CN (4.0 mL) at 25 °C. The reaction solution was stirred for 6 h and filtered to remove excess solid PhIO and insoluble impurities. The Mn^V−oxo complex was also generated in quantitative yield by using solid PhIO and used for further characterization and reactivity studies. Moreover, the addition of peroxides such as hydrogen peroxide, cumene hydroperoxide, and *tert*-butyl hydroperoxide to the solution containing [Mn^{III}(TAML)]$^-$ afforded quantitative yield of **1**.[3b−d] Anal. Calcd (found) for $C_{43}H_{42}MnN_4O_5P$ (**1**): C, 66.15 (66.32); H, 5.42 (5.25); N, 7.18 (7.22).

The Sc^{3+} ion bound Mn^V(O) complex, [Mn^V(O)(TAML)]$^-$−(Sc^{3+}) (**2**), was prepared by adding 1.2 equiv of Sc^{3+} ion to the solution of **1** in CH_3CN at −20 °C. Further addition of Sc^{3+} ions (up to 20 equiv) to the solution of **2** did not show spectral changes any more, indicating the binding of only one Sc^{3+} ion to the Mn^V(O) complex, which is different from the previously reported Mn^{IV}(O) complexes that bind two Sc^{3+} ions.[7b]

X-ray Structural Analysis. To improve the quality of the single crystal of **1**, the cation exchange from Li$^+$ to PPh$_4^+$ has been performed by introducing PPh_4Cl into the solution containing **1**-Li. **1**-PPh$_4$ was obtained by filtration of the reaction solution. Single crystals of **1**-PPh$_4$ suitable for X-ray crystallographic analysis were obtained by slow diffusion of Et_2O into a saturated CH_3CN solution of **1**-PPh$_4$. These crystals were taken from the solution by a nylon loop (Hampton Research Co.) on a handmade copper plate and mounted on a goniometer head in a N_2 cryostream. The diffraction data for **1**-PPh$_4$ were collected at 100 K on a Bruker SMART AXS diffractometer equipped with a monochromator in the Mo Kα (λ = 0.71073 Å) incident beam. The CCD data were integrated and scaled using the Bruker-SAINT software package, and the structure was solved and refined using SHELXTL V 6.12.[32] Hydrogen atoms were located in the calculated positions. The crystallographic data and selected bond distances and angles for **1**-PPh$_4$ are listed in Tables S1 and S2, respectively. Crystallographic data for [Mn^V(O)(TAML)]$^-$ is available as Supporting Information. In addition, CCDC-1028627 contains the supplementary crystallographic data for this paper. These data can be obtained free of charge via www.ccdc.cam.ac.uk/data_request/cif (or from the Cambridge Crystallographic Data Centre, 12, Union Road, Cambridge CB2 1EZ, U.K.; fax (+44) 1223-336-033; or deposit@ccdc.cam.ac.uk).

X-ray Absorption Spectroscopy. The Mn K-edge X-ray absorption spectra of the starting material [Mn^{III}(TAML)]$^-$, [Mn^V(O)(TAML)]$^-$ (**1**), and [Mn^V(O)(TAML)]$^-$−Sc^{3+} (**2**) complexes were measured at the Stanford Synchrotron Radiation Lightsource (SSRL) on the unfocused 20-pole 2 T wiggler side-station beamline 7-3 under nonstandard ring conditions of 3 GeV and ∼100 mA (low-alpha operations mode at SSRL). A Si(220) double crystal monochromator was used for energy selection. A Rh-coated harmonic rejection mirror was used on beamline 7-3 to reject components of higher harmonics. The monochromator was further detuned by 30% to eliminate higher harmonics and to reduce beam damage on the high-valent samples (**1** and **2**). All complexes were measured as solutions, which were transferred into 2 mm Delrin XAS cells with 70 μm Kapton tape windows under synthesis conditions and were immediately frozen after preparation and stored under liquid N_2. During data collection, samples were maintained at a constant temperature of ∼10−15 K using an Oxford Instruments CF 1208 liquid helium cryostat. Data were measured to k = 12 Å^{-1} (fluorescence mode) using a Canberra Ge 30-element array detector. Internal energy calibration was accomplished by simultaneous measurement of the absorption of a Mn foil placed between two ionization chambers situated after the sample. The first inflection point of the foil spectrum was fixed at 6539.0 eV. The samples were monitored for photoreduction and a fresh spot was chosen for data collection after every four scans. However, no visual change in the rising edge energy position or the intense pre-edge feature associated with the Mn^V(O) complexes, **1** and **2**, was observed over successive scans, indicating that all the samples were resistant to photoreduction under the reduced current experimental conditions. Data presented here are 22-scan average for [Mn^{III}(TAML)]$^-$, 24-scan average for **1**, and 12-scan average for **2**. Data were processed by fitting a second-order polynomial to the pre-edge region and subtracting this from the entire spectrum as background. A three-region spline of orders 2, 3, and 3 was used to model the smoothly decaying postedge region. The data were normalized by subtracting the cubic spline and assigning the edge jump to 1.0 at 6555 eV using the Pyspline[33] program. Data were then renormalized in Kaleidagraph for comparison and quantification purposes.

Theoretical EXAFS signals $\chi(k)$ were calculated by using FEFF (Macintosh version 8.4).[34−36] Starting structural models for [Mn^{III}(TAML)]$^-$ and **1** were obtained from crystal structures, and models for **2** were generated by modifying the crystal structure of **1** in Avogadro[37] (by inclusion of a Sc^{3+} ion). The input structure was improved based on preliminary EXAFS fit parameters to generate more accurate theoretical EXAFS signals. Data fitting was performed in EXAFSPAK.[38] The structural parameters varied during the fitting process were the bond distance (R) and the bond variance σ^2, which is related to the Debye−Waller factor resulting from thermal motion, and static disorder of the absorbing and scattering atoms. The nonstructural parameter ΔE_0 (E_0 is the energy at which k = 0) was also allowed to vary but was restricted to a common value for every component in a given fit. Coordination numbers were systematically varied in the course of the fit but were fixed within a given fit.

DFT Methods. Calculations were done with density functional theory (DFT)[39] using the Gaussian 09 package[40] and the B3LYP[41] functional. Optimizations and single-point frequency calculations were done with the LACVP basis set[23] (except for S, which required 6-311+G*), while single-point energy evaluations were done using the

DOI: 10.1021/jacs.6b03874
J. Am. Chem. Soc. 2016, 138, 8523−8532

Def2-TZVPP basis set.[42] All calculations (including the optimizations) were done in solvent (acetonitrile) using the CPCM scheme.[43] Single-point dispersion was calculated with DFT-D3 program.[44] The quoted energy value in the text is the electronic energy value at B3LYP/Def2-TZVPP//B3LYP/LACVP level, rather than the free energies due to issues with the reliability of free energy values (the free energies are available in Table S5).[45] TD-DFT[46] calculations were performed at the uB3LYP/LACVP level with 50 roots.

Spectral Redox Titration for the Equilibrium Constant (K_{et}). Redox titration of electron transfer from dibromoferrocene (Br_2Fc) to **2** (0.25 mM) was examined in the various concentrations of Br_2Fc (0.010−0.70 mM) in CH_3CN at −20 °C using a Hewlett-Packard 8453 photodiode-array spectrometer with a quartz cuvette (path length = 10 mm). Typically, a deaerated CH_3CN solution of Br_2Fc (0.010−0.70 mM) was added to a deaerated CH_3CN solution containing **2** (0.25 mM). The concentration of dibromoferrocenium ion (Br_2Fc^+) was determined from the absorption band at λ = 700 nm due to Br_2Fc^+ (ε_1 = 400 M^{-1} cm^{-1}) and **2** (ε_2 = 0) following eq 5 derived from eq 4, where $[\mathbf{2}]_0$ is the initial concentration of **2**.

$$\mathrm{Abs}_{700} = \varepsilon_1[\mathrm{Br_2Fc^+}] + \varepsilon_2[\mathbf{2}] = \varepsilon_1[\mathrm{Br_2Fc^+}] \quad (4)$$

$$[\mathrm{Br_2Fc^+}] = \mathrm{Abs}_{700}/\varepsilon_1 \quad (5)$$

The ε_1 value (400 M^{-1} cm^{-1}) of Br_2Fc^+ at 700 nm was also confirmed by the electron-transfer oxidation of dibromoferrocene with cerium(IV) ammonium nitrate in CH_3CN at −20 °C.

The expression used for determination of K_{et} was derived according to our previous work.[47] The equilibrium constant (K_{et}) in eq 1 is expressed by eq 6,

$$K_{et} = [\mathrm{Mn^{IV}(O)}] \times [\mathrm{Br_2Fc^+}]/([\mathbf{2}] \times [\mathrm{Br_2Fc}]) \quad (6)$$

where $Mn^{IV}(O)$ denotes the one-electron-reduced species of **2**. Equation 7 is derived from eq 6, where $[Mn^{IV}(O)] = [Br_2Fc^+]$, $[Br_2Fc]_0 = [Br_2Fc] + [Br_2Fc^+]$, and $[\mathbf{2}]_0 = [\mathbf{2}] + [Mn^{IV}(O)]$. $[\mathbf{2}]_0$ and $[Br_2Fc]_0$ are the initial concentrations of $[\mathbf{2}]$ and $[Br_2Fc]$, respectively.

$$1/K_{et} = ([\mathbf{2}]_0 - [\mathrm{Br_2Fc^+}]) \times ([\mathrm{Br_2Fc}]_0 - [\mathrm{Br_2Fc^+}])/[\mathrm{Br_2Fc^+}]^2$$
$$= ([\mathbf{2}]_0/[\mathrm{Br_2Fc^+}] - 1) \times ([\mathrm{Br_2Fc}]_0/[(\mathrm{Br_2Fc^+}] - 1) \quad (7)$$

Equation 8 is derived from eq 7, where $\alpha = [Mn^{IV}(O)]/[\mathbf{2}]_0 = [Br_2Fc^+]/[\mathbf{2}]_0$.

$$(\alpha^{-1} - 1)^{-1} = K_{et}([\mathrm{Br_2Fc}]_0/\alpha[\mathbf{2}]_0 - 1) \quad (8)$$

Finally, the K_{et} value of 47 is determined from the slope of the linear plot between $(\alpha^{-1} - 1)^{-1}$ and $[Br_2Fc]_0/\alpha[\mathbf{2}]_0 - 1$ (Figure S22).

Kinetic Measurements and Product Analysis. Reactions were run in a 1 cm UV cuvette and followed by monitoring UV−vis spectral changes of reaction solutions, and rate constants were determined under pseudo-first-order conditions (e.g., [substrate]/$[Mn^V(O)]$ > 10) by fitting the changes in absorbance at 430 nm for **1** and at 465 nm for **2**, respectively. Fast reaction traces were collected at 465 nm due to **2**, using a 1.0 cm optical path length of stopped-flow cell. Reaction traces were collected, and the time dependence of the absorbance at 465 nm was fitted with single exponential function to give k_{obs} (s^{-1}) under the pseudo-first-order conditions. The raw kinetic data were treated with KinetAsyst 3 (Hi-Tech Scientific) and Specfit/32 Global Analysis System software from Spectrum Software Associates. O_2-activation reaction rates in the presence of excess amount of cycloalkene were monitored by the formation of an absorption band at 430 nm due to **1** in air-saturated acetone at room temperature. Kinetic isotope effect was determined by comparing the formation rates of **1** in the presence of cyclohexene and cyclohexene-d_{10}. **2** was in situ prepared by treating **1** with 1.2 equiv of Sc^{3+} ion in CH_3CN at −20 °C, and the resulting solution was directly used in the reaction with triphenylphosphine (PPh_3). Temperature-dependent kinetic experiments were performed with **1** (0.10 mM) at a given temperature in order to compare with the reactivity of **2** in the oxidation of PPh_3 in CH_3CN at −20 °C. Rates of electron transfer from ferrocene derivatives to **2** were monitored by the formation and decay of absorption bands due to ferrocenium ions and **2**, respectively. All kinetic measurements were carried out under pseudo-first-order conditions where concentrations of ferrocene derivatives were maintained to be in >10-fold excess of that of **2**. All reactions were run at least in triplicate, and the data reported represent the average of these reactions. Products formed in the O_2-activation reactions by $[Mn^{III}(TAML)]^-$ with olefins, which were carried out under air atmosphere, were analyzed by GC and GC−MS. Decane (1.0 mM) was used as an internal standard. In the formation of **1** by $Li(CH_3OH)_2[Mn^{III}(TAML)(CH_3OH)]$ with cyclohexene in the presence of O_2 in acetone at 25 °C, cyclohex-2-enol and cyclohex-2-enone were obtained as products with the yields of 21(3)% and 32(3)%, respectively. Products formed in the oxidation reaction of PPh_3 by **1** and **2** were also analyzed by GC. A solution of PPh_3 (50 mM) was added directly to solutions of **1** (1.0 mM) at 25 °C and **2** (1.0 mM) at −20 °C, resulting in triphenylphosphine oxide being obtained as the sole product with 85(6)% and 90(5)% yields (based on the intermediate generated), respectively.

■ ASSOCIATED CONTENT

Supporting Information

The Supporting Information is available free of charge on the ACS Publications website at DOI: 10.1021/jacs.6b03874.

Figures S1−S23, Tables S1−S8, and coordinates of the DFT-calculated structure (PDF)

Crystallographic data for $[Mn^V(O)(TAML)]^-$ (CIF)

■ AUTHOR INFORMATION

Corresponding Authors

*wwnam@ewha.ac.kr

*fukuzumi@chem.eng.osaka-u.ac.jp

*ritis@slac.stanford.edu

Notes

The authors declare no competing financial interest.

■ ACKNOWLEDGMENTS

The authors acknowledge financial support from the NRF of Korea through CRI (NRF-2012R1A3A2048842 to W.N.), GRL (NRF-2010-00353 to W.N.), and MSIP (NRF-2013R1A1A2062737 to K.-B.C.) and from the MEXT of Japan through JSPS KAKENHI (Grant no. 16H02268 to S.F.). Stanford Synchrotron Radiation Lightsource (SSRL) operations are funded by the US Department of Energy (DOE)—Basic Energy Sciences. The SSRL Structural Molecular Biology program is supported by NIH—National Centre for Research Resources (P41 RR001209) and DOE—Biological Environmental Research (R.S.).

■ REFERENCES

(1) (a) Neu, H. M.; Baglia, R. A.; Goldberg, D. P. *Acc. Chem. Res.* **2015**, *48*, 2754. (b) Liu, W.; Groves, T. *Acc. Chem. Res.* **2015**, *48*, 1727. (c) Chen, Z.; Yin, G. *Chem. Soc. Rev.* **2015**, *44*, 1083. (d) Ray, K.; Heims, F.; Schwalbe, M.; Nam, W. *Curr. Opin. Chem. Biol.* **2015**, *25*, 159.

(2) (a) Young, K. J.; Brennan, B. J.; Tagore, R.; Brudvig, G. W. *Acc. Chem. Res.* **2015**, *48*, 567. (b) Yano, J.; Yachandra, V. *Chem. Rev.* **2014**, *114*, 4175. (c) Cox, N.; Pantazis, D. A.; Neese, F.; Lubitz, W. *Acc. Chem. Res.* **2013**, *46*, 1588. (d) Rivalta, I.; Brudvig, G. W.; Batista, V. S. *Curr. Opin. Chem. Biol.* **2012**, *16*, 11. (e) Zhang, C.; Chen, C.; Dong, H.; Shen, J.-R.; Dau, H.; Zhao, J. *Science* **2015**, *348*, 690. (f) Suga, M.; Akita, F.; Hirata, K.; Ueno, G.; Murakami, H.; Nakajima, Y.; Shimizu, T.; Yamashita, K.; Yamamoto, M.; Ago, H.; Shen, J.-R. *Nature* **2015**, *517*, 99. (g) Kanady, J. S.; Tsui, E. Y.; Day, M. W.; Agapie, T. *Science* **2011**, *333*, 733. (h) Sala, X.; Maji, S.; Bofill, R.; García-Antón, J.; Escriche, L.; Llobet, A. *Acc. Chem. Res.* **2014**, *47*, 504.

DOI: 10.1021/jacs.6b03874
J. Am. Chem. Soc. 2016, 138, 8523−8532

(3) (a) Popescu, D.-L.; Chanda, A.; Stadler, M.; de Oliveira, F. T.; Ryabov, A. D.; Münck, E.; Bominaar, E. L.; Collins, T. J. *Coord. Chem. Rev.* **2008**, *252*, 2050. (b) Miller, C. G.; Gordon-Wylie, S. W.; Horwitz, C. P.; Strazisar, S. A.; Peraino, D. K.; Clark, G. R.; Weintraub, S. T.; Collins, T. J. *J. Am. Chem. Soc.* **1998**, *120*, 11540. (c) Collins, T. J.; Powell, R. D.; Slebodnick, C.; Uffelman, E. S. *J. Am. Chem. Soc.* **1990**, *112*, 899. (d) Collins, T. J.; Gordon-Wylie, S. W. *J. Am. Chem. Soc.* **1989**, *111*, 4511.

(4) Yin, G. *Acc. Chem. Res.* **2013**, *46*, 483.

(5) (a) Kurahashi, T.; Kikuchi, A.; Shiro, Y.; Hada, M.; Fujii, H. *Inorg. Chem.* **2010**, *49*, 6664. (b) Wu, X.; Seo, M. S.; Davis, K. M.; Lee, Y.-M.; Chen, J.; Cho, K.-B.; Pushkar, Y. N.; Nam, W. *J. Am. Chem. Soc.* **2011**, *133*, 20088. (c) Garcia-Bosch, I.; Company, A.; Cady, C. W.; Styring, S.; Browne, W. R.; Ribas, X.; Costas, M. *Angew. Chem., Int. Ed.* **2011**, *50*, 5648. (d) Taguchi, T.; Gupta, R.; Lassalle-Kaiser, B.; Boyce, D. W.; Yachandra, V. K.; Tolman, W. B.; Yano, J.; Hendrich, M. P.; Borovik, A. S. *J. Am. Chem. Soc.* **2012**, *134*, 1996. (e) Leto, D. F.; Ingram, R.; Day, V. W.; Jackson, T. A. *Chem. Commun.* **2013**, *49*, 5378. (f) Gupta, R.; Taguchi, T.; Lassalle-Kaiser, B.; Bominaar, E. L.; Yano, J.; Hendrich, M. P.; Borovik, A. S. *Proc. Natl. Acad. Sci. U. S. A.* **2015**, *112*, 5319.

(6) (a) Prokop, K. A.; Goldberg, D. P. *J. Am. Chem. Soc.* **2012**, *134*, 8014. (b) Jung, J.; Ohkubo, K.; Prokop-Prigge, K. A.; Neu, H. M.; Goldberg, D. P.; Fukuzumi, S. *Inorg. Chem.* **2013**, *52*, 13594.

(7) (a) Nam, W.; Lee, Y.-M.; Fukuzumi, S. *Acc. Chem. Res.* **2014**, *47*, 1146. (b) Chen, J.; Lee, Y.-M.; Davis, K. M.; Wu, X.; Seo, M. S.; Cho, K.-B.; Yoon, H.; Park, Y. J.; Fukuzumi, S.; Pushkar, Y. N.; Nam, W. *J. Am. Chem. Soc.* **2013**, *135*, 6388. (c) Yoon, H.; Lee, Y.-M.; Wu, X.; Cho, K.-B.; Sarangi, R.; Nam, W.; Fukuzumi, S. *J. Am. Chem. Soc.* **2013**, *135*, 9186. (d) Chen, J.; Yoon, H.; Lee, Y.-M.; Seo, M. S.; Sarangi, R.; Fukuzumi, S.; Nam, W. *Chem. Sci.* **2015**, *6*, 3624. (e) Fukuzumi, S.; Ohkubo, K.; Lee, Y.-M.; Nam, W. *Chem. - Eur. J.* **2015**, *21*, 17548.

(8) (a) Leeladee, P.; Baglia, R. A.; Prokop, K. A.; Latifi, R.; de Visser, S. P.; Goldberg, D. P. *J. Am. Chem. Soc.* **2012**, *134*, 10397. (b) Baglia, R. A.; Dürr, M.; Ivanović-Burmazović, I.; Goldberg, D. P. *Inorg. Chem.* **2014**, *53*, 5893. (c) Zaragoza, J. P. T.; Baglia, R. A.; Siegler, M. A.; Goldberg, D. P. *J. Am. Chem. Soc.* **2015**, *137*, 6531.

(9) (a) Pfaff, F. F.; Kundu, S.; Risch, M.; Pandian, S.; Heims, F.; Pryjomska-Ray, I.; Haack, P.; Metzinger, R.; Bill, E.; Dau, H.; Comba, P.; Ray, K. *Angew. Chem., Int. Ed.* **2011**, *50*, 1711. (b) Hong, S.; Pfaff, F. F.; Kwon, E.; Wang, Y.; Seo, M.-S.; Bill, E.; Ray, K.; Nam, W. *Angew. Chem., Int. Ed.* **2014**, *53*, 10403.

(10) (a) Bang, S.; Lee, Y.-M.; Hong, S.; Cho, K.-B.; Nishida, Y.; Seo, M. S.; Sarangi, R.; Fukuzumi, S.; Nam, W. *Nat. Chem.* **2014**, *6*, 934. (b) Lee, Y.-M.; Bang, S.; Kim, Y. M.; Cho, J.; Hong, S.; Nomura, T.; Ogura, T.; Troeppner, O.; Ivanović-Burmazović, I.; Sarangi, R.; Fukuzumi, S.; Nam, W. *Chem. Sci.* **2013**, *4*, 3917.

(11) (a) Du, H.; Lo, P.-K.; Hu, Z.; Liang, H.; Lau, K.-C.; Wang, Y.-N.; Lam, W. W. Y.; Lau, T.-C. *Chem. Commun.* **2011**, *47*, 7143. (b) Yiu, S.-M.; Man, W.-L.; Lau, T.-C. *J. Am. Chem. Soc.* **2008**, *130*, 10821. (c) Lam, W. W. Y.; Yiu, S.-M.; Lee, J. M. N.; Yau, S. K. Y.; Kwong, H.-K.; Lau, T.-C.; Liu, D.; Lin, Z. *J. Am. Chem. Soc.* **2006**, *128*, 2851.

(12) (a) Chen, Z.; Yang, L.; Choe, C.; Lv, Z.; Yin, G. *Chem. Commun.* **2015**, *51*, 1874. (b) Choe, C.; Yang, L.; Lv, Z.; Mo, W.; Chen, Z.; Li, G.; Yin, G. *Dalton Trans.* **2015**, *44*, 9182. (c) Dong, L.; Wang, Y.; Lv, Y.; Chen, Z.; Mei, F.; Xiong, H.; Yin, G. *Inorg. Chem.* **2013**, *52*, 5418.

(13) (a) Cook, S. A.; Borovik, A. S. *Acc. Chem. Res.* **2015**, *48*, 2407. (b) Park, Y. J.; Cook, S. A.; Sickerman, N. S.; Sano, Y.; Ziller, J. W.; Borovik, A. S. *Chem. Sci.* **2013**, *4*, 717. (c) Park, Y. J.; Ziller, J. W.; Borovik, A. S. *J. Am. Chem. Soc.* **2011**, *133*, 9258.

(14) (a) Gross, Z.; Golubkov, G.; Simkhovich, L. *Angew. Chem., Int. Ed.* **2000**, *39*, 4045. (b) Lansky, D. E.; Mandimutsira, B.; Ramdhanie, B.; Clausén, M.; Penner-Hahn, J.; Zvyagin, S. A.; Telser, J.; Krzystek, J.; Zhan, R.; Ou, Z.; Kadish, K. M.; Zakharov, L.; Rheingold, A. L.; Goldberg, D. P. *Inorg. Chem.* **2005**, *44*, 4485. (c) Kim, S. H.; Park, H.; Seo, M. S.; Kubo, M.; Ogura, T.; Klajn, J.; Gryko, D. T.; Valentine, J. S.; Nam, W. *J. Am. Chem. Soc.* **2010**, *132*, 14030.

(15) (a) Morimoto, Y.; Lee, Y.-M.; Nam, W.; Fukuzumi, S. *Chem. Commun.* **2013**, *49*, 2500. (b) Comba, P.; Lee, Y.-M.; Nam, W.; Waleska, A. *Chem. Commun.* **2014**, *50*, 412. (c) Nishida, Y.; Lee, Y.-M.; Nam, W.; Fukuzumi, S. *J. Am. Chem. Soc.* **2014**, *136*, 8042.

(16) Yamada, M.; Karlin, K. D.; Fukuzumi, S. *Chem. Sci.* **2016**, *7*, 2856.

(17) Luo, Y.-R. *Handbook of bond dissociation energies in organic compounds*; CRC Press: New York, 2003.

(18) (a) Traylor, T. G.; Traylor, P. S. In *Active Oxygen in Biochemistry*; Valentine, J. S., Foote, C. S., Greenberg, A., Liebman, J. F., Eds.; Blackie Academic and Professional: London, 1995; pp 84−187. (b) Kim, S. O.; Sastri, C. V.; Seo, M. S.; Kim, J.; Nam, W. *J. Am. Chem. Soc.* **2005**, *127*, 4178. (c) Ghiladi, R. A.; Kretzer, R. M.; Guzei, I.; Rheingold, A. L.; Neuhold, Y.-M.; Hatwell, K. R.; Zuberbühler, A. D.; Karlin, K. D. *Inorg. Chem.* **2001**, *40*, 5754−5767.

(19) We tried our best to capture a putative Mn^{IV}−superoxo species, but we were not able to detect it spectroscopically because this intermediate is a very short-lived species. Based on the kinetics, detection of no intermediates, and a large kinetic isotope effect, the formation of the Mn^{IV}−superoxo complex is proposed to be a highly uphill reaction, followed by the rate-determining hydrogen abstraction from cyclohexene by the Mn^{IV}−superoxo complex in competition with the back reaction to regenerate the Mn^{III} complex (Scheme 1). In such a case, intermediates, such as the Mn^{IV}−superoxo complex or the Mn^{III}−hydroperoxo complex, cannot be captured.

(20) Lee, Y.-M.; Hong, S.; Morimoto, Y.; Shin, W.; Fukuzumi, S.; Nam, W. *J. Am. Chem. Soc.* **2010**, *132*, 10668.

(21) We synthesized **2** in CH_3CN, since we only observed the formation of **2** in CH_3CN. There was no spectral change upon addition of Sc^{3+} ion into the solution of **1** in acetone.

(22) Yano, J.; Robblee, J.; Pushkar, Y.; Marcus, M. A.; Bendix, J.; Workman, J. M.; Collins, T. J.; Solomon, E. I.; DeBeer George, S.; Yachandra, V. K. *J. Am. Chem. Soc.* **2007**, *129*, 12989.

(23) (a) The LACVP basis set uses Pople style 6-31G basis set on all atoms except transition metals, where an ECP is used as defined in the quantum chemistry program *Jaguar*, version 7.7; Schrödinger, LLC: New York, 2010. See also: (b) Hay, P. J.; Wadt, W. R. *J. Chem. Phys.* **1985**, *82*, 299.

(24) NIST Computational Chemistry Comparison and Benchmark Database, NIST Standard Reference Database Number 101 Release 17b, September 2015, Editor: Johnson, R. D., III. http://cccbdb.nist.gov/.

(25) (a) Lee, Y.-M.; Kotani, H.; Suenobu, T.; Nam, W.; Fukuzumi, S. *J. Am. Chem. Soc.* **2008**, *130*, 434. (b) Yoon, H.; Morimoto, Y.; Lee, Y.-M.; Nam, W.; Fukuzumi, S. *Chem. Commun.* **2012**, *48*, 11187.

(26) (a) Marcus, R. A. *Annu. Rev. Phys. Chem.* **1964**, *15*, 155. (b) Marcus, R. A. *Angew. Chem., Int. Ed. Engl.* **1993**, *32*, 1111.

(27) Fukuzumi, S. *Coord. Chem. Rev.* **2013**, *257*, 1564.

(28) Armarego, W. L. F.; Chai, C. L. L. In *Purification of Laboratory Chemicals*, 6th ed.; Pergamon Press: Oxford, 2009.

(29) Saltzman, H.; Sharefkin, J. G. In *Organic Syntheses*; Wiley: New York, 1973; Collect. Vol. *V*, pp 658.

(30) (a) Collins, T. J.; Gordon-Wylie, S. W. *J. Am. Chem. Soc.* **1989**, *111*, 4511. (b) Hong, S.; Sutherlin, K. D.; Park, J.; Kwon, E.; Siegler, M. A.; Solomon, E. I.; Nam, W. *Nat. Commun.* **2014**, *5*, 5440. (c) Horwitz, C. P.; Ghosh, A. U.S. Pat. Appl. Publ. (US 20040167329 A1 20040826), 2004.

(31) Mann, C. K.; Barnes, K. K. In *Electrochemical Reactions in Non-aqueous Systems*; Mercel Dekker: New York, 1970.

(32) Sheldrick, G. M. In *SHELXTL/PC Version 6.12 for Windows XP*; Bruker AXS Inc.: Madison, WI, 2001.

(33) Tenderholt, A.; Hedman, B.; Hodgson, K. O. *PySpline: A Modern, Cross-Platform Program for the Processing of Raw Averaged XAS Edge and EXAFS Data; X-ray Absorption Fine Structure - XAFS13* **2006**, *882*, 105.

(34) Mustre de Leon, J.; Rehr, J. J.; Zabinsky, S. I.; Albers, R. C. *Phys. Rev. B: Condens. Matter Mater. Phys.* **1991**, *44*, 4146.

(35) Rehr, J. J.; Mustre de Leon, J.; Zabinsky, S. I.; Albers, R. C. *J. Am. Chem. Soc.* **1991**, *113*, 5135.

DOI: 10.1021/jacs.6b03874
J. Am. Chem. Soc. 2016, 138, 8523−8532

(36) Zabinsky, S. I.; Rehr, J. J.; Ankudinov, A.; Albers, R. C.; Eller, M. J. *Phys. Rev. B: Condens. Matter Mater. Phys.* **1995**, *52*, 2995.
(37) *Avogadro: an open-source molecular builder and visualization tool. Version 1.XX.* http://avogadro.openmolecules.net/.
(38) George, G. N. *EXAFSPAK*; Stanford Synchrotron Radiation Laboratory, Stanford Linear Accelerator Center: Stanford, CA, 2000.
(39) Kohn, W.; Sham, L. J. *Phys. Rev.* **1965**, *140*, A1133.
(40) Frisch, M. J.; Trucks, G. W.; Schlegel, H. B.; Scuseria, G. E.; Robb, M. A.; Cheeseman, J. R.; Scalmani, G.; Barone, V.; Mennucci, B.; Petersson, G. A.; Nakatsuji, H.; Caricato, M.; Li, X.; Hratchian, H. P.; Izmaylov, A. F.; Bloino, J.; Zheng, G.; Sonnenberg, J. L.; Hada, M.; Ehara, M.; Toyota, K.; Fukuda, R.; Hasegawa, J.; Ishida, M.; Nakajima, T.; Honda, Y.; Kitao, O.; Nakai, H.; Vreven, T.; Montgomery, J. A.; Peralta, J. E.; Ogliaro, F.; Bearpark, M.; Heyd, J. J.; Brothers, E.; Kudin, K. N.; Staroverov, V. N.; Kobayashi, R.; Normand, J.; Raghavachari, K.; Rendell, A.; Burant, J. C.; Iyengar, S. S.; Tomasi, J.; Cossi, M.; Rega, N.; Millam, J. M.; Klene, M.; Knox, J. E.; Cross, J. B.; Bakken, V.; Adamo, C.; Jaramillo, J.; Gomperts, R.; Stratmann, R. E.; Yazyev, O.; Austin, A. J.; Cammi, R.; Pomelli, C.; Ochterski, J. W.; Martin, R. L.; Morokuma, K.; Zakrzewski, V. G.; Voth, G. A.; Salvador, P.; Dannenberg, J. J.; Dapprich, S.; Daniels, A. D.; Farkas; Foresman, J. B.; Ortiz, J. V; Cioslowski, J.; Fox, D. J. *Gaussian 09, Revision D.01*; 2009.
(41) (a) Becke, A. D. *Phys. Rev. A: At., Mol., Opt. Phys.* **1988**, *38*, 3098. (b) Becke, A. D. *J. Chem. Phys.* **1993**, *98*, 1372. (c) Becke, A. D. *J. Chem. Phys.* **1993**, *98*, 5648. (d) Lee, C.; Yang, W.; Parr, R. G. *Phys. Rev. B: Condens. Matter Mater. Phys.* **1988**, *37*, 785.
(42) Weigend, F.; Ahlrichs, R. *Phys. Chem. Chem. Phys.* **2005**, *7*, 3297.
(43) (a) Barone, V.; Cossi, M. *J. Phys. Chem. A* **1998**, *102*, 1995. (b) Cossi, M.; Rega, N.; Scalmani, G.; Barone, V. *J. Comput. Chem.* **2003**, *24*, 669.
(44) Grimme, S.; Antony, J.; Ehrlich, S.; Krieg, H. *J. Chem. Phys.* **2010**, *132*, 154104.
(45) Ho, J.; Klamt, A.; Coote, M. L. *J. Phys. Chem. A* **2010**, *114*, 13442.
(46) Runge, E.; Gross, E. K. U. *Phys. Rev. Lett.* **1984**, *52*, 997.
(47) Fukuzumi, S.; Kondo, Y.; Mochizuki, S.; Tanaka, T. *J. Chem. Soc., Perkin Trans. 2* **1989**, 1753.

DOI: 10.1021/jacs.6b03874
J. Am. Chem. Soc. 2016, 138, 8523−8532